Science
AAAS

Supplementary Materials for

A hippocampal circuit mechanism to balance memory reactivation during sleep

Lindsay A. Karaba *et al*.

Corresponding author: Azahara Oliva, aog35@cornell.edu

Science **385**, 738 (2024)
DOI: 10.1126/science.ado5708

The PDF file includes:

Materials and Methods

Surgical procedures

Mice (adult C57, ~25-30g, 3-6 months old) were kept in the vivarium on a 12 hour light / dark cycle. They were housed with a maximum of 5 per cage before surgery and individually afterwards. All experiments conformed to guidelines established by the National Institutes of Health and have been approved by the Cornell University Institutional Animal Care and Use Committee. Silicon probes were implanted as previously described (*11*). Briefly, mice were anesthetized with isoflurane and coordinates were taken following stereotaxic guidance after which craniotomies were performed. Silicon probes of 64 channels (NeuroNexus) or 128 channels (Diagnostic Biochips) were mounted on a micro-drive (Cambridge Neurotech) to allow accurate adjustment of the vertical position of the electrodes after implantation. A stainless-steel wire connected to a thin wire (California Wires) was inserted over the cerebellum and cemented in place with metabond. A layer of metabond was applied to the full of the skull avoiding the craniotomies, thinner inside and thicker on the outer side of the skull forming a ring, over which four flaps of copper mesh were attached. The electrodes were then inserted right above the target regions (aided by the micromanipulators), one aimed at targeting CA1 on the left hemisphere (AP:-1.94, LAT:-1.5) and the other aimed at targeting CA2 over the right hemisphere CA2 (AP:-1.94, LAT:2.15). Once in place, the microdrives were cemented over the skull. Once probes had been inserted and drives cemented to the skull, craniotomies were sealed with artificial dura-gel. Finally, the four flaps of copper mesh were bent upwards and soldered between them to provide stability and shielding the implant. The ground wire from the cerebellum was connected to the ground wires of the two electrodes and all together to the copper mesh.

Virus Injections

Stock AAV and EnvA-Pseudotyped Rabies preparations were acquired from Addgene and Salk Institute Gene Transfer, Targeting and Therapeutics Viral Vector Core. For behavioral optogenetic inhibition (see Optogenetics and Behavioral Manipulation) of Sncg+ interneurons (Fig. 5), AAV-nEF-Coff/Fon-Arch3.3-p2a-EYFP (2.01 x 10^{13} gc/ml) was injected in SNCG-Flp mice at coordinates: AP-1.94, ML±1.5mm, DV 1.0mm. A full virus titer was used, and injections were done bilaterally (400nl's each side) using Nanoject III programmable Nanoliter Injector (Drummond Scientific Company 3-000-207). Animals were given two weeks to allow for virus expression and recovery before being implanted with optic fibers (see Optogenetics and Behavioral Manipulations) and silicon probes (see Surgical Procedures). For optogenetic tagging (Fig. 4), AAV-hnEF-Coff/Fon-hChR2(H134R)-EYFP (2.6 x 10^{13} gc/ml) was injected in SNCG-Flp mice at the following coordinates: AP-1.94mm, ML±1.5mm, DV 1.0mm. Full virus titer was used, and injections were done bilaterally (400nl's each side) as described previously (*25*). To inhibit CA2 pyramidal neurons, we injected AAV-CAG -Flex-Arch3.0-GFP (2.0 x 10^{13} gc/ml) into the dorsal CA2 of Amigo2-Cre mice with 400nl's bilaterally at the following coordinates AP-1.94, ML±2.0mm, DV1.7mm, as previously described (*11*, *54*).

To identify local hippocampal inputs onto CCK+ basket cells, we employed EnvA-Pseudotyeped Rabies tracing that takes advantage of rabies-virus-mediated retrograde trans-synaptic tracing (*28*) to identify monosynaptic inputs onto a specific cell type (*29*, *30*). First, SNCG-Flp animals were injected with two AAVs 1) AAV-CAG-FLEX(FRT)-TC (TVA-mCherry, 2.69 x 10^{13} gc/ml) and 2) AAV-CAG-fDIO-oG-WPRE-SV40PA (1.74 x 10^{13} gc/ml) to target SNCG positive CCK basket cells with TVA-receptor and optimized rabies glycoprotein. AAV's were injected at three sites 1) AP:-1.70, ML:-1.25mm, DV:-1.00mm; 2) AP:-1.94, ML-

1.50mm, DV: -1.0mm; 3) AP:-2.10, ML:-2.0mm, DV:-1.00mm with 400nl injections of combination of both AAV viruses, either 1:1 TVA:OG or 1:2 TVA:OG. After two to three weeks, animals were injected at the same three injection sites with 400nl's of EnvA-G-Deleted-Rabies-eGFP (1.34 x 10^8 gc/ml). This virus is a pseudotyped rabies virus lacking rabies glycoprotein that contains virus envelope A from avian sarcoma leukosis virus (EnvA). The resulting EnvA-G-Deleted Rabies will bind to TVA receptor in SNCG CCK basket cells via EnvA binding (*55*) and complete the rabies virus via the addition of optimized rabies glycoprotein (*28–30*). As a result, completion of the rabies virus in SCNG CCK+ basket cells (mCherry+ EGFP+, "starter cells") will be achieved. This will allow for labeling cells with monosynaptic inputs onto SNCG CCK+ basket cells (mCherry- eGFP+, "input cells"). After, EnvA-G-Deleted-Rabies-eGFP animals were allowed one week of recovery and incubation before euthanizing and imaging brain slices (see Tissue processing and immunohistochemistry).

The pAAV-nEF-Coff/Fon-Arch3.3-p2a-EYFP virus was a gift from Karl Deisseroth & INTRSECT 2.0 Project (Addgene viral prep # 137150-AAV8; http://n2t.net/addgene:137150; RRID:Addgene_137150) (*56*).

The pAAV-hnEF Coff/Fon hChR2(H134R)-EYFP virus was a gift from Karl Deisseroth (Addgene viral prep # 55649-AAV8; http://n2t.net/addgene:55649; RRID:Addgene_55649) (*57*).

The CAG-FLEx(FRT)-TC plasmid was a gift from Liqun Luo (Addgene plasmid # 67827; http://n2t.net/addgene:67827; RRID:Addgene_67827) and the AAV-CAG-fDIO-oG-WPRE-SV40pA plasmid was a gift from Edward Callaway (Addgene plasmid # 74291; http://n2t.net/addgene:74291 ; RRID:Addgene_74291). Both viruses were packaged by Salk Institute Gene Transfer, Targeting and Therapeutics Viral Vector Core.

The plasmid EnvA-G-Deleted-Rabies-eGFP was a gift from Edward Callaway (Addgene plasmid # 32635 ; http://n2t.net/addgene:32635 ; RRID:Addgene_32635) packaged by Salk Institute Gene Transfer, Targeting and Therapeutics Viral Vector Core.

The plasmid pAAV-CAG -Flex-Arch3.0-GFP was a gift from Edward Boyden (Addgene plasmid #222222; http://n2t.net/addgene:22222; RRID: Addgene_222222) (*58*).

Behavioral tasks

Before surgery, animals were exposed to the different mazes (open field and T-Maze) to avoid neophobia after implants. After surgery, mice were handled daily and accommodated to the experimenter, recording room, and cables for at least a week before the start of the experiments. Brain signals were recorded during an object's displacement memory task (*17*), a social memory task (*11*), and a T-Maze alternation memory task (*16*), as well as during sleep before and after the tasks. On occasional days, only long sleep sessions were recorded.

In the object's displacement memory task, mice (n=8) were trained to explore two objects during three consecutive trials of 5 minutes, preceded by a 5-minute exploration trial of the empty open field. Pre-sleep and post-sleep sessions of 2-4 hours preceded and followed these trials. After post-sleep, animals were tested in a single trial of 10 minutes where one object had been moved to a new location of the open field (*17*).

In the social memory recognition test, mice (n=7) were trained to explore two novel stimulus animals confined under pencil cups in two of the corners of the open field. The stimulus animals had been previously exposed to being under the pencil cups. Two consecutive trials of 5 minutes each were conducted. In between these trials, the positions of the stimulus mice were swapped (*11*). Pre-sleep and post-sleep sessions of 2 hours preceded and followed these trials.

After post-sleep, animals were tested in a single trial of 10 minutes where one new stimulus mouse was introduced under one of the cups.

In the T-Maze alternation task, mice (n=4) were trained to run in a figure eight maze with 5 seconds delay, starting at the beginning of the center stem and having to alternate between the left and right arms of the maze in each trial. Upon completion of a correct trial, a reward (chocolate sprinkle) was provided at the end of the side stems. Pre-sleep and post-sleep sessions of 2-3 hours preceded and followed the maze trials (~20-40 trials or ~30 minutes running) (*16*).

For all tasks, the behavior of the mouse was recorded with an overhead camera (Basler) at 30 Hz and the position of the animal was later extracted using DeepLabCut (*59*).

Typically, and if recording quality/stability allowed it, mice were recorded in multiple tasks in an order chosen at random. Mice were not recorded for two consecutive days in the objects' displacement or social memory tasks.

A discrimination index was used to estimate memory performance in the object displacement task and calculated as time spent exploring the moved object minus time spent exploring the stationary object divided by the total time of object's exploration in the test trial. Sessions were mice explored less than 5 s were excluded.

Optogenetics and behavioral manipulations

Transgenic animals were used to optogenetically target pyramidal cells or cholecystokinin expressing interneurons (CCK) in the hippocampus. CaMKIIα-Cre homozygous mice (Jackson Laboratory, #0005359) were crossed with Ai32 homozygous (Jackson Laboratory, #012569) that encode ChR2 in a Cre-dependent manner (offspring referred as CamKII-ChR2). First-generation offspring animals were used for optogenetic manipulations (see "Optogenetics and Behavioral Manipulations"). To target CCK interneurons, SNCG-Flp (Jackson Laboratory, #034424) mice were used (*25*). SNCG-Flp were kept in heterozygous crosses and both homozygous and heterozygous were used for optogenetic manipulations.

SWRs were generated as previously described (*11*, *21*, *22*, *60*). Specifically, CamKII-ChR2 animals were implanted (see "Surgical Procedures") with two silicon probes with custom glued optical fibers of 200 µm (Thorlab FT200UMT). The electrode on the right hemisphere was aimed at targeting CA2 with the most lateral shank (with the fiber on top of the most medial shank over CA1) and the electrode (and fiber) on the left was aimed at targeting CA1. SWR's were generated with 60-ms, low intensity (0.5-2mW) light pulses using a trapezoid 10-ms taper-on and 20-ms taper-off square pulses to minimize light artifact (*11*, *21*, *22*, *60*). The pulse for stimulation was produced using Spike2 in a Cambridge Electronic Device -CED- Limited Edition (Power 1401) to control a Laser Diode (Osram 470nm wavelength) triggered by a current source (Thor Lab, LDC 240C). Intensity was manually adjusted during a few trials in a session prior to experiments until optogenetic stimulation continually produced SWRs. For SWR generation experiments, SWRs were generated at a rate equivalent to the endogenous SWR rate (~0.3 Hz) (*11*).

For barrage disruption, we silenced CCK interneurons continuously during 2s after a period of 2s after SWRs detection, following the optimal timing of BARRs occurrence with respect to SWRs based on the cross-correlogram between the two events. Based on the average number of BARRs that occurred within this period of time after SWRs, we estimate that ~60% of BARRs should have been silenced. Despite this approach not being a real-time BARR silencing, green light pulses in Sncg+ mice injected with Flp-dependent Arch were able to silence the firing of Sncg+ cells (fig. S3L and fig. S10E), whose firing mediated BARR-

associated inhibition. SNCG-Flp animals were implanted with a 64-channel silicon probe with a custom glued optical fiber of 200 µm and a contralateral optical fiber of 200 µm (Thorlab FT200UMT), both targeting the CA1 region of the hippocampus. High intensity (2 to 5 mW) green light squared pulses were applied. The pulse was defined in Spike2 and a Cambridge Electronic Device -CED- Limited Edition (Power 1401) was used to control a Laser Diode (Osram 520 nm wavelength) triggered by a current source (Thor Lab, LDC 240C).

To inhibit CA2-specific pyramidal neurons, we injected Cre-dependent Arch, as described previously (see "Virus Injections"). Two weeks after injections, mice were implanted with silicon probes as described previously (see "Surgical Procedures"), along with custom glued optical fibers (200 µm, Thorlab FT200UMT). We silenced CA2 pyramidal cells during putative barrage times (see "Optogenetics and behavioral manipulations"). Specifically, we applied light 2s after SWR detection for a period of 2s of high intensity (2 to 5mW) of green light square pulses (540nm). Pulses were defined by online SWR detection using Spike2 in a CED Limited Edition (Power 1401) to control a Primatix Optogenetics-LED-STSI module (Primatix Limited).

Recording system and preprocessing of data

An Intan RHD2000 interface board or Intan Recording Controller was used for recordings. The sampling rate used was set at 20000 Hz. Both amplification and digitization were done in the head stage (Intan Technologies). Data were visualized using the Intan recording software or Neuroscope (Neurosuite). LFP analyses, including SWR detection and sleep scoring, were done in the down-sampled signal at 1250 Hz.

Tissue processing and immunohistochemistry

After experiments were terminated, mice were deeply anesthetized and kept under high-flow (4-5%) isoflurane anesthesia. They were then perfused transcardially with 0.9% phosphate buffer saline (PBS) solution followed by 4% paraformaldehyde (PFA) solution. Brains were kept in PFA for 24 hours and, if necessary, in PBS afterwards until further processing. Brains were then sectioned into 70-µm thick slices (Leica Vibratome, 2000). Additionally, immunolabeling for the CA2 region-specific marker PCP4 (*61*) was performed. Specifically, slices were washed three times in PBS-Triton 0.5% (PBX-Tx) solution and then blocked with 10% bovine serum albumin in PBS-Tx 0.5%, then blocked with 10% bovine serum albumin in PBS-Tx and incubated overnight at 4ºC temperature with the primary antibody solution containing rabbit anti-PCP4 (1:1000, Sigma-Aldrich Cat# HPA005792, RRID:AB 1855086). After three washes in PBS-Tx, sections were incubated for 2 hours at room temperature with goat anti-rabbit Alexa Fluor 647 (1:500, Thermo Fisher Scientific Cat# A-21245, RRID:AB_2535813). Finally, sections were washed and mounted on glass slides with fluorescence medium (Fluoroshield with DAPI – F6057, Sigma, USA). Immunostained slices were examined, and images were acquired with a confocal microscope (Zeiss LSM 800). To amplify AAV-CAG-FLEX(FRT)-TC (TVA-mCherry), an mCherry fused Alexa Fluor 594 antibody (1:500, Fisher Scientific Catalog No. 50-113-80889) was used to stain Rabies retrograde tracing slices before imaging (see “Virus Injections”).

Spike sorting and single unit classification

Spike sorting was performed semi-automatically using KiloSort (*62*) (https://github.com/cortex-lab/ KiloSort), followed by manual curation using the software Phy (github.com/kwikteam/phy) and custom designed plugins (https://github.com/petersenpeter/phy-

plugins) to obtain well-isolated single units. Cluster quality was assessed by manual inspection of waveforms and auto-correlograms, and by the isolation distance metric. Multiunit, noise clusters, or poorly isolated units were discarded from the analysis. Well-isolated units were classified into putative cell types using the Matlab package Cell Explorer (petersenpeter.github.io/Cell-Explorer) (*63*). Spiking features such as autocorrelogram, spike waveform, and putative monosynaptic connections derived from short-term crosscorrelograms were used to select and characterize well-isolated units. Three cell types were assigned: putative pyramidal cells, narrow waveform interneurons, and wide waveform interneurons. The two key metrics used for this separation were burst index and trough-to-peak latency (*64*). Burst index was determined by calculating the average number of spikes in the 3–5 ms bins of the spike autocorrelogram divided by the average number of spikes in the 200–300 ms bins. To calculate the trough-to-peak latency, the average waveforms were taken from the recording site with the maximum amplitude for the averaged waveforms of a given unit. For further quantifications, well-isolated cells with at least 100 spikes in a given session were included in the analyses.

SWR detection and spike content analysis

For SWR detection, the wide-band signal from a CA1 pyramidal layer channel was filtered (difference-of-Gaussians; zero-lag, linear phase FIR), and instantaneous power was calculated by clipping at 4 SDs, rectifying, and lowpass filtering (*11*, *12*, *19–22*). The low-pass filter cut-off was at a frequency corresponding to p cycles of the mean bandpass (for 80-250 Hz band-pass, the low-pass was 55 Hz). Subsequently, the power of the non-clipped signal was computed, and all events exceeding 4 SDs from the mean were detected. The events were then expanded until the non-clipped power fell below 1 SD; short events (< 15 ms) were discarded. Sharp waves were detected separately using LFP from a CA1 str. radiatum channel, filtered with band-pass filter boundaries (5-40 Hz). LFP events of a minimum duration of 20 ms and a maximum of 400 ms exceeding 2.5 SD of the background signal were included as candidate SWRs.

SWRs firing rate was calculated as the number of spikes within SWRs divided by the cumulative SWR duration for the session. The firing rate gain during SWRs was calculated as the increase in firing rate within SWRs compared to the baseline firing rate (outside SWRs). The probability of participation of individual units in SWRs was defined as the number of events in which a neuron fired at least one spike during the SWR divided by the total number of SWRs detected. Peri-SWRs firing histograms were constructed using averaged single units z-scored firing rates.

SWRs firing rate gain was calculated as the firing rate within a given SWR where the neuron was active. An average was taken for pre- and post-sleep SWRs for the whole population of CA1 and/or CA2 neurons. The gain was then estimated subtracting the pre-sleep to the post-sleep firing rate and dividing this by the sum of the two.

BARR detection and spike content analysis

BARRs were detected as transient increases in coordinated spike bursting within a subpopulation of CA2 pyramidal cells. First, a threshold was used for extracting the cells that can sustain burst-like spiking persistently (“flagged CA2 pyramidal cells”, with a frequency higher than 30 Hz during more than 300 ms). Using this subpopulation of CA2 pyramidal cells, a binned (5 ms per bin) spike-train was constructed and convolved with a Gaussian kernel (20 ms). A candidate event was defined if multiunit spiking activity crossed a given threshold (between 3

to 5 standard deviations) over the mean for a minimum of 200 ms during NREM epochs (or other states if specified). BARR events were further restricted to requiring a minimum of 20% of the previously identified CA2 pyramidal cells to fire 5-7 spikes in an event. Single unit firing rate in BARRs was calculated as the number of spikes within BARRs divided by the cumulative BARR duration for the session. The firing rate gain during BARRs was calculated as the increase in firing rate within BARRs compared to baseline firing rate (outside BARRs and outside SWRs but within non-REM sleep). The probability of participation of individual units in BARRs was defined as the number of events in which a neuron fired at least five spikes during the BARR divided by the total number of BARRs detected. Peri-BARR firing histograms were constructed using averaged single unit z-scored firing rates.

BARRs firing rate gain was calculated as the firing rate within a given SWR where the neuron was active. An average was taken for pre- and post-sleep BARRs for the whole population of CA1 and/or CA2 neurons. The gain was then estimated subtracting the pre-sleep to the post-sleep firing rate and dividing this by the sum of the two.

Task-encoding and place cell analyses

"Task active cells" were defined as the top 75th percentile of pyramidal cells that increased their firing rate during the task over their own baseline (calculated in pre-sleep) (*11*, *65*). They were compared against the rest of the cells ("non-task encoding" or "other" cells).

For place cell analyses, spike trains and animal's position vectors were binned into 3 cm wide segments of the camera field projected onto the floor of the maze, creating a raw map of spike counts and space occupancy. A gaussian kernel (SD = 3 cm) was applied to both raw maps of spike and occupancy, and a smoothed rate map was constructed by dividing the spike map by the occupancy map. Independent rate maps were constructed for the different running directions in the mazes. Only periods in which the animal velocity was greater than 4 cm/s were included. A place cell was defined as a pyramidal cell with a peak firing rate > 4 Hz and a spatial information content significantly ($p<0.01$) greater than a null distribution created from 500 random spike train shuffles. We estimated the spatial information in place cell firing by calculating the bits per spike as previously described (*19*):

$$Information = \sum_{i=1}^{N} P_i \frac{\lambda_i}{\lambda} log_2 \frac{\lambda_i}{\lambda} \quad (1)$$

where the environment is divided into spatial bins i = 1,…, N; P_i is the occupancy probability of bin i; λ_i is the mean firing rate for bin i, and λ is the overall mean firing rate of the cell.

Classification of deep and superficial pyramidal cells

For the classification of pyramidal cells based on the radial position of their soma, the relative depth of each electrode along the pyramidal layer was calculated based on the stereotypical depth profile of SWRs as the probe transects the pyramidal layer. The slow envelope of the SWR showed a positive polarity above the pyramidal layer and started reversing polarity right across the middle of the pyramidal layer (*19*, *44*, *45*). Below the middle of the pyramidal layer (superficial sublayer), SWRs' envelope showed a negative polarity. The amplitude of this envelope gradually increased, peaking in the middle of the stratum radiatum (i.e., the sharp wave). The relative depth of each electrode was determined in relation to the channel of polarity reversal (the middle of the layer: 0um), considering the inter-electrode distance for each recording session. The position of the soma of each pyramidal cell was determined next to the electrode with the largest amplitude waveforms within that shank.

Reactivation, pairwise, cell assembly and population synchrony analyses

Explained Variance (EV) was calculated using previously described methods (*5*, *11*, *19*, *20*, *65*). For each session, a population spiking activity vector was computed for the different stages of the session (pre-sleep, task, and post-sleep). The final explained variance metric estimates the variance in the post-sleep stage that is explained by the task activity, considering pre-existing correlations already present in the pre-sleep activity:

$$EV = \left(\frac{r_{C,C_{POST}} - r_{C,C_{PRE}} r_{C_{POST},C_{PRE}}}{\sqrt{(1-r^2_{C,C_{PRE}})(1-r^2_{C_{POST},C_{PRE}})}}\right)^2 \quad (2)$$

where C is the correlation matrix during the task and C_{PRE} and C_{POST} are the correlation matrices during SWRs (or BARRs). $r_{A,B}$ represents the correlation coefficient between the pairwise correlation matrices A and B. As a control value, the reverse explained variance (REV) was used, where C_{PRE} and C_{POST} conditions were interchanged.

In the pairwise correlation analyses, we conducted a partial regression by first computing a linear regression between C_{POST} and C_{PRE} to account for the variance in C_{POST} that was already present during the PRE condition and later computed a correlation between the resultant residuals and the task (*19*). For cell assembly (activity patterns) detection, we used an unsupervised statistical method based on first principal component analysis (PCA) detection, followed by principal components analysis (ICA) as previously described (*11*, *18–20*, *66*). First, spike trains for each neuron are binned (25 ms bin) for the whole session. During the timing of the task, assemblies are calculated based on principal components whose eigenvalues exceed the threshold for random firing correlations (using a Marčenko-Pastur distribution). Next, independent component analysis (using the fast-ICA algorithm) was applied to determine the vector of weights with which neuron's firing contributes to each assembly. The strength of each assembly is activation for a given time bin *k* was calculated as:

$$S_{ik} = Z_k^T \, P \, Z_k \quad (3)$$

where Z is the activity matrix of the z-scored firing rate of each unit, and P is the outer product of the component *i*'s weights with the diagonal set to zero, so that isolated spikes from individual units do not contribute to S. Assembly-activations were defined as peaks exceeding $R_{threshold} > 5$. The activation strength within events (SWRs or BARRs) was calculated as the mean peak activation value of events that occurred during a whole stage (i.e., pre-sleep or post-sleep). A given cell was considered part of an assembly if its weight exceeded the mean weight of the assembly by two standard deviations (*11*, *66*, *67*).

Population synchrony was derived by calculating the proportion of pyramidal cells that contributed at least one spike in each post-task sleep SWR. A single population synchrony metric per recording session was then taken by averaging these proportions over each post-task sleep SWR. Thus, values closer to 1 indicate greater synchrony and values closer to 0 indicate lower synchrony.

Average inter-spike intervals (ISI) were estimated as the time distance between two consecutive spikes (*68*) for all SWRs with more than three spikes, thus smaller values (shorter ISI) indicate higher synchrony.

Local field potentials and spectral analysis

To obtain the LFP power spectrums, a channel of the region of interest (CA1 or CA2) was selected and then clipped in peri-event time windows for all the SWRs and BARRs separately. A wavelet spectrogram was calculated for each event (an example was selected for

each wavelet color plot) and then averaged for all events (in the average quantification plot). The complex wavelet transform (CWT) was used (MATLAB, The MathWorks, Inc., Natick, MA) (*69*) to build each individual spectrogram.

To obtain the point-process spectrograms of the spiking activity we computed a multi-taper estimation and their Fast Fourier Transforms (FFT) and applied it to the spectrogram windows (200 ms window surrounding each event) (chronux.org).

Independent Component Analysis

To separate the LFP signals into its different contributing sources, we used independent component analysis (ICA) (*15*) to isolate spatially segregated stable patterns of activity from a mixed signal recorded with a laminar array of electrodes. Applied to linear profiles of LFPs, it can separate physiologically meaningful sources that can be attributed to known anatomical pathways or underlying circuits, as has been demonstrated for the rat hippocampus (*15*, 70), mice visual cortex (*71*) and rat motor cortex (*72*). Briefly, the multichannel LFP signal $X \in R^{N\times T}$ is modeled as:

$$X = AS \quad (4)$$

where each column of the mixing matrix $A \in R^{N\times M}$ represents the spatial profile of pathway-specific contribution, and each row of $S \in R^{M\times T}$ is the pathway specific source activity, with N, T, M being channel number, recording length and number of independent components respectively. ICA also finds the demixing matrix $W = \{w_1;...;w_M\} \in R^{M\times N}$, such that $S = WX$, where each row w_i demixed the LFP signal to their pathway activity s_i, and by definition, $WA = I$. Since the scale of W and A is indeterminable (*73*), each column in A is normalized to be the unit norm vector whose largest loading is set to be negative, and W is then rescaled accordingly. To extract the sources contributing to the LFP during SWRs and BARRs, A and W were found by applying ICA to spatially contiguous LFP channels after a temporal difference ($x_{t+1} - x_t$) to decrease the contribution of the lower frequencies to the LFP, as previously described (*15*, 70, *74*, *75*), then the activity S is obtained from the original LFP signal with $S = WX$. We computed ICA on the full probe shank crossing through the CA2 region. The components from all sessions from different animals were extracted and aligned based on their spatial profile in relation to the spatial distribution of the CA2 units.

Sleep and brain states' classification

First, we extracted the low pass signal (1250 Hz) from the wide-band data as described above for LFP analyses. Broadband LFP, narrow-band theta frequency LFP, and estimated electromyogram (EMG) were used for estimating the brain states (*40*, *76*). Spectrograms were computed from broadband LFPs using a fast Fourier transform with 10 seconds and sliding windows of 1 second. Principal component analyses were then computed after a Z-transform (1-100 Hz) of the spectrogram. The first component reflected power in the low (< 20 Hz) frequency range, with oppositely weighted power at higher (> 32 Hz) frequencies. For theta epochs, a good quality channel with visually high theta power was manually selected. Theta dominance was quantified as the ratio of powers in the 5-10 Hz and 2-16 Hz frequency bands. Electromyogram (EMG) from local muscles was estimated from the neural data as the zero-lag correlation between 300-600 Hz filtered signals (Butterworth filter at 300 – 600Hz with a filter padding between 275 – 625 Hz) between recording sites (*40*, *70*). Pairwise Pearson correlations between pairs of channels located in non-adjacent probe shanks were calculated. The mean of all correlations in time bins of 0.5 s was calculated and used as an EMG score. EMG typically

corresponded to motion periods (calculated as the derivative of the position of the animal estimated by pose video markers) (*59*). Evaluating all time points with these three variables (LFP, theta and EMG) consistently resulted in three clusters that were used to identify brain states. The cluster with high LFP and low EMG was classified as NREM; the cluster with high theta/low EMG was classified as REM and the cluster with low broadband LFP, high EMG and bouts of theta was taken as the waking state. For most analyses in this study only NREM periods were used. After the automatic scores for different sleep stages were obtained, all states were reviewed by the experimenters and redetected if necessary (i.e., long periods of EMG corresponding to bad quality channels or periods of high movement introducing noise in the neural data).

Statistical Analyses

Statistical analyses were performed with MATLAB and Python functions or custom-made scripts. No specific analysis was used to estimate a minimal population sample or group size, but the number of animals, sessions, and recorded cells were larger or similar to those employed in previous works doing the same type of manipulations (*11*, *15*, *19–22*, *77*). The unit of analysis was single neurons, assemblies, or number of events (SWRs or BARRs). In some analyses, the unit of analysis was sessions and is stated in the text. Unless otherwise noted, non-parametric two-tailed Wilcoxon rank-sum (equivalent to Mann-Whitney U-test) or Wilcoxon signed-rank test was used for unpaired and paired data comparisons respectively. Statistical significance is indicated by asterisks: *$p<0.05$, **$p<0.01$ and ***$p<0.001$.

For single cells, assemblies, spike content and synchrony analyses, only sessions with more than 7 pyramidal cells from each subregion (CA1 and CA2) per recording were considered. Similarly, for SWRs or BARRs analyses, only sessions with at least 100 events were considered. For behavior quantification, sessions where mice explored less than 5 seconds during training or recall were not considered.

In the boxplots, the central line indicates the median, with top and bottom edges indicating 75^{th} and 25^{th} percentiles respectively. Whiskers extend to the most extreme data points not considered outliers. Outliers are not included in most plots but are included in statistical analysis.

When confidence intervals of a shuffled sample of the data are used, they indicate the 95^{th} percentile over the total of the shuffled samples.
If data points for a given analysis are no more (or less) than ten samples, each sample (data point) is displayed along with boxplots of the group.

Due to experimental constraints of optogenetic experiments (i.e., animal removing fiber attachment that can damage the implant, light remaining on for too long due to failure or artifacts, what could cause epilepsy, etc.), the experimenter was not blind to these manipulations. Instead, in these cases, data were analyzed by a different researcher other than the one collecting the data.

If the same animal was tested in different version tasks or used for different manipulations (i.e., Sncg+ silencing during SWRs and Sncg+ silencing during BARRs), the temporal order of the different manipulations followed a randomized order.

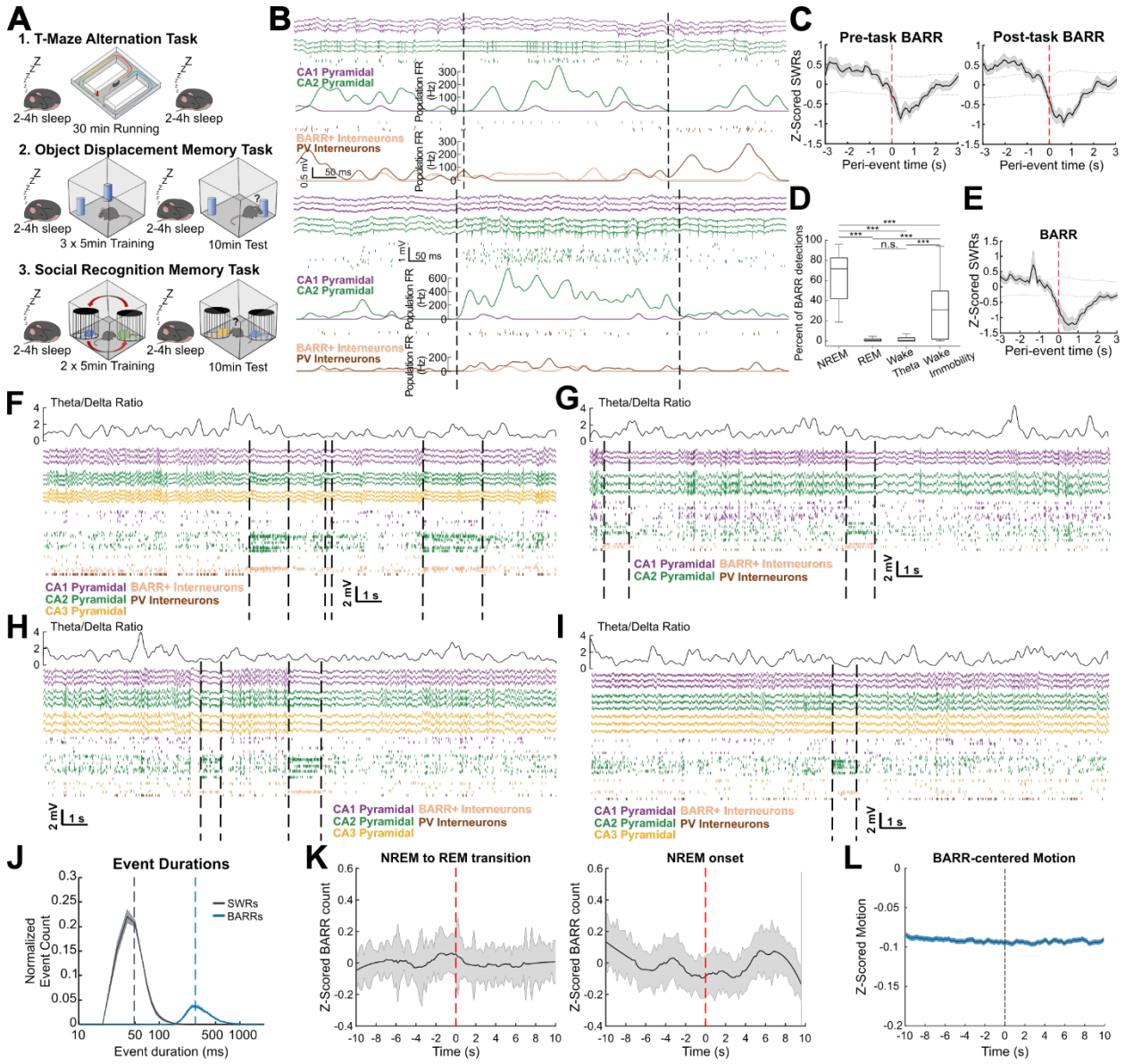

Fig. S1. Schematic of behavioral tasks and BARR examples. (A) Schematic of the different behavioral paradigms used. Cup positions are rotated for the second training session in the Social Recognition Memory Task. **(B)** Representative examples of BARRs from different animals. LFP traces from CA1 and CA2 are on top and raster plots with CA1 and CA2 pyramidal cells, PV-like interneurons' and BARR+ interneurons' firing below. Curves display the average firing rate of neurons from each subtype. **(C)** Averaged cross-correlogram between BARRs and SWRs in pre-task sleep (left, n = 50 sessions from n = 10 mice) and post-task sleep (right, n = 50 sessions from n = 10 mice). Dashed lines indicate 95% C.I. from shuffled data ($p < 0.001$, Wilcoxon rank sum test). **(D)** Percent of BARR detections per sleep state (n = 52 sessions in n = 10 mice). **(E)** Averaged cross-correlogram between BARRs and SWRs detected during waking periods (n = 52 sessions from n = 10 mice). Dashed lines indicate 95% C.I. from shuffled data ($p < 0.001$, Wilcoxon rank sum test). **(F-I)** Representative examples of BARRs from different animals on an extended timescale. LFP theta-band power and delta-band power is plotted on top. Below are LFP traces from CA1, CA2, and CA3 regions. Raster plots including CA1, CA2, and CA3

pyramidal cells, as well as putative PV+ interneurons and BARR+ interneurons, are below. Each row in the raster represents one neuron and each tick represents one spike. Periods with one or more BARRs are indicated by the dashed black lines. **(J)** Average duration of BARRs and SWRs. Note a much larger duration of BARRs compared to SWRs ($p < 0.001$, n = 45,301 BARRs / 464,828 SWRs from n = 52 sessions in n = 10 mice; Wilcoxon-rank sum test). **(K)** Averaged cross-correlogram between BARRs and NREM-to-REM transition times (left, n = 52 sessions from 10 mice), and BARRs and NREM onset times (right, n = 52 sessions from 10 mice). **(L)** Z-scored motion (derived from accelerometer data) averaged on the onset of BARRs (n = 52 sessions from 10 mice). */**/*** $p < 0.05/0.01/0.001$ Wilcoxon-rank test unless otherwise noted.

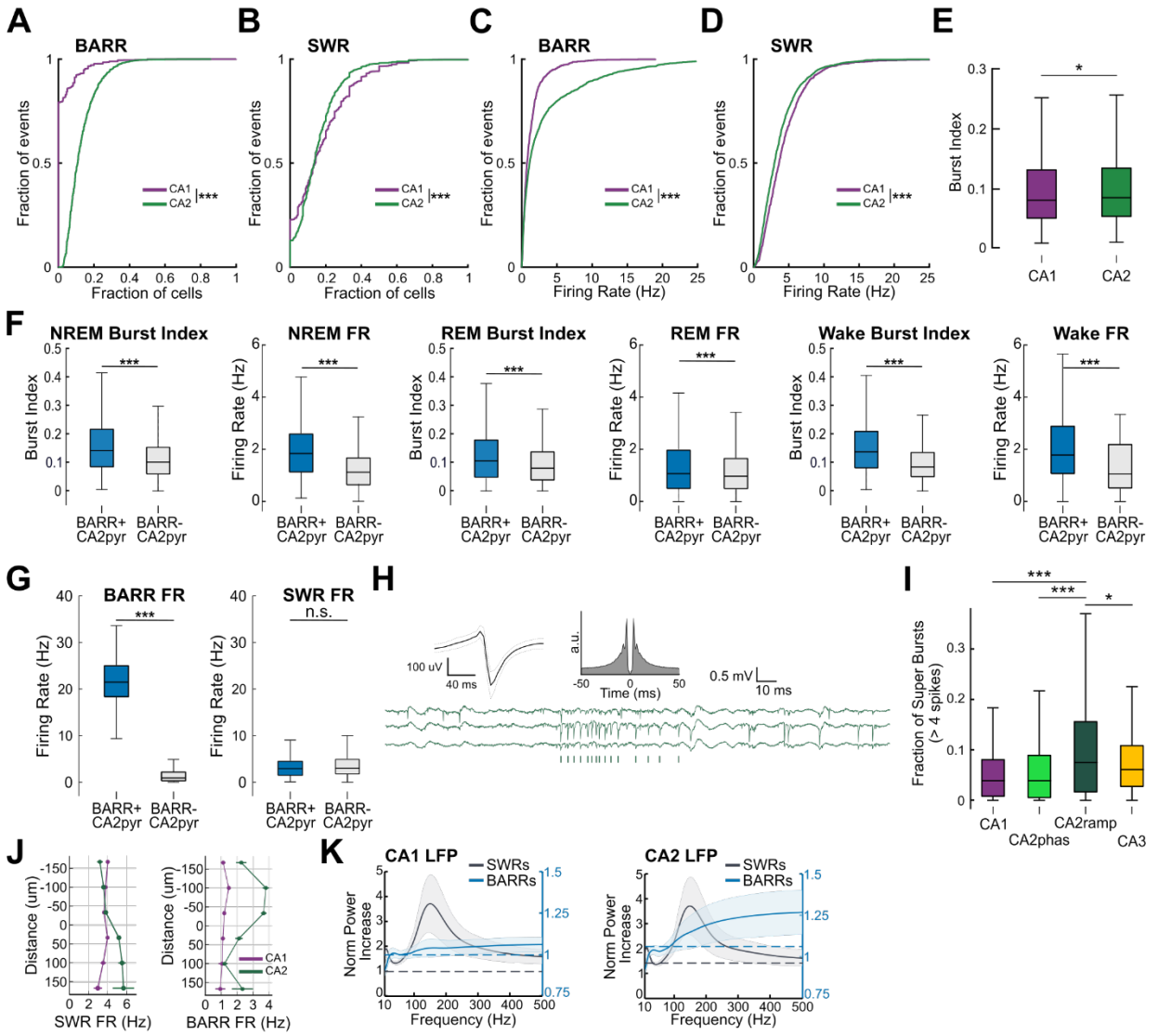

Fig. S2. Single cell firing properties of pyramidal cells during BARRs and SWRs as a comparison. (A) Cumulative fraction of CA1 and CA2 pyramidal cells active in BARRs ($p < 0.001$ for CA1 versus CA2 comparison, n = 45,301 BARRs). **(B)** Cumulative fraction of CA1 and CA2 pyramidal cells active in SWRs ($p < 0.001$ for CA1 versus CA2 comparison, n = 464,828 SWRs). **(C)** Cumulative firing rate probability of CA1 and CA2 pyramidal cells during BARRs ($p < 0.001$ for CA1 versus CA2 comparison). **(D)** Cumulative firing rate probability of CA1 and CA2 pyramidal cells during SWRs ($p < 0.001$ for CA1 versus CA2 comparison, n = 959 / 2,128 CA1 / CA2 cells respectively). **(E)** Burst index of CA1 and CA2 pyramidal cells ($p < 0.05$ for CA1 versus CA2 comparison). **(F)** Burst Index and firing rate (FR) for BARR+/- CA2 pyramidal neurons (CA2pyr) during NREM, REM, and Wake periods ($p < 0.001$ for NREM, REM, and Wake Burst Index and FR comparison of BARR+ versus BARR- CA2 pyramidal cells, n = 542 / 1618 BARR+/- CA2 pyramidal cells respectively, n = 52 sessions in n = 10 mice). **(G)** Firing rate of BARR+/- cells during BARRs (left, $p < 0.001$, n = 542 / 1618 BARR+/- CA2 pyramidal cells, n = 52 sessions in n = 10 mice) or SWRs (right, $p = 0.364$, n = 542 / 1618 BARR+/- CA2 pyramidal cells respectively, n = 52 sessions in n = 10 mice). **(H)** Example of a CA2 pyramidal cell firing a burst of >10 spikes. **(I)** Fraction of super bursts of >4 spikes for

pyramidal cells from different subregions ($p < 0.001$, $p < 0.001$, and $p < 0.05$ for CA2ramp versus CA1, CA2phas, and CA3 respectively). **(J)** Average firing rate of CA1 and CA2 pyramidal cells during SWRs (left) and BARRs (right) located across different positions within the radial axis ($p < 0.001$ and $p < 0.05$ for SWRs and BARRs respectively, ANOVA of region (CA1 and CA2) by distance interaction). **(K)** Normalized power for all frequencies during BARRs (blue) and SWRs (black) for all sessions ($p > 0.05$ for CA1 versus CA2 SWRs, $n = 451,291$; $p < 0.001$ for CA1 versus CA2 BARRs, $n = 45,281$). */**/*** $p < 0.05/0.01/0.001$ Wilcoxon-rank test unless otherwise noted.

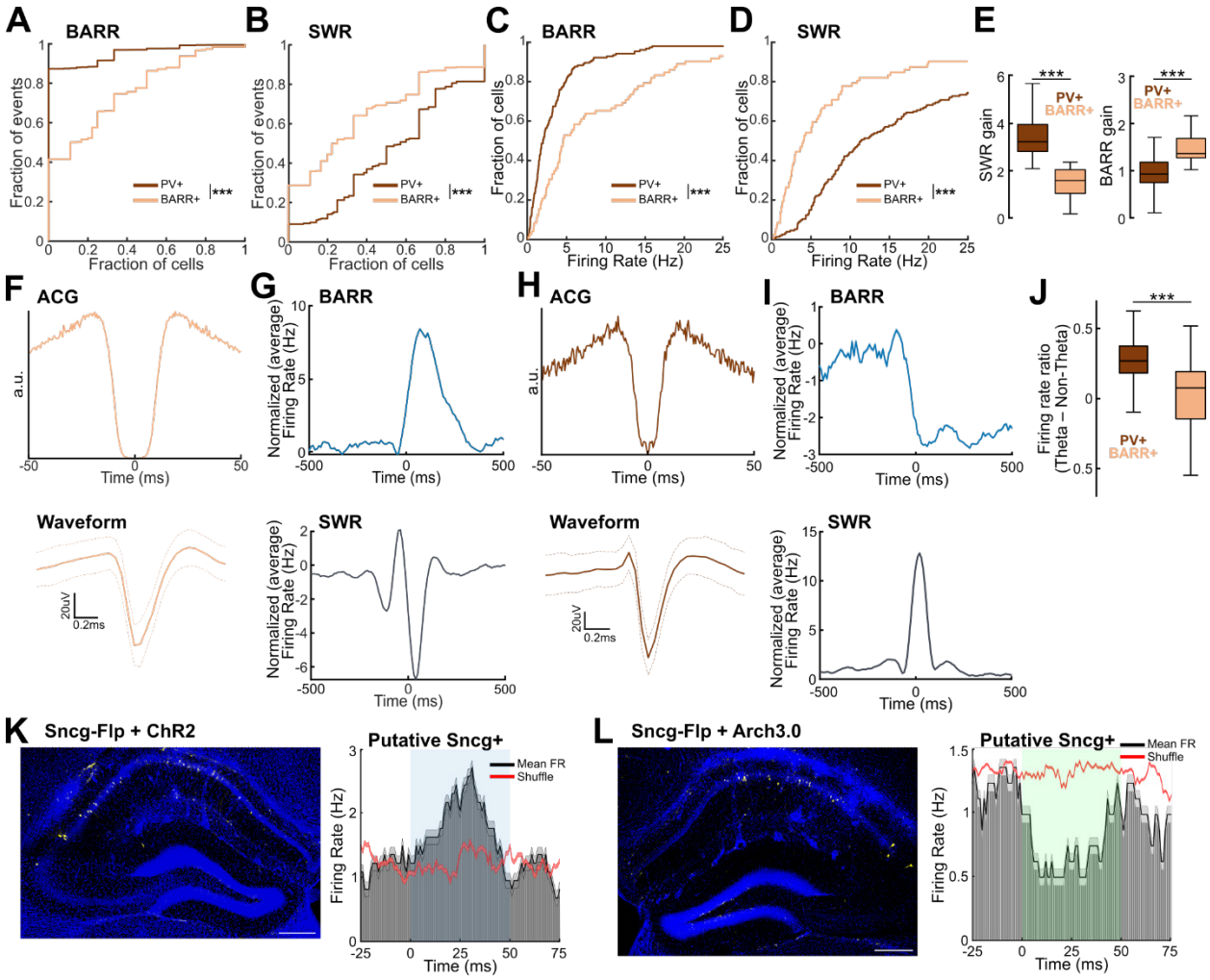

Fig. S3: Single cell firing properties of interneurons during BARRs and SWRs as a comparison. (A) Cumulative fraction of BARR+ interneurons and putative PV+ interneurons active in BARRs ($p < 0.001$; n = 10127 / 27172 BARRs for BARR+ and putative PV+ respectively). **(B)** Cumulative fraction of BARR+ interneurons and PV+ interneurons active in SWRs ($p < 0.001$; n = 70887 / 210811 SWRs for BARR+ and putative PV+ respectively). **(C)** Cumulative firing rate probability of BARR+ interneurons and PV+ interneurons active during BARRs ($p < 0.001$; n = 71 / 154 for putative PV+ and BARR+ respectively). **(D)** Cumulative firing rate probability of BARR+ interneurons and putative PV+ interneurons active during SWRs ($p < 0.001$; n = 71 / 154 for putative PV+ and BARR+ respectively). **(E)** Firing rate gain during SWRs and BARRs for both groups of interneurons ($p < 0.001$ for SWR gain and $p < 0.001$ for BARR gain comparisons). **(F)** Autocorrelogram (top) and waveform (bottom) of an example BARR+ interneuron. **(G)** Average normalized firing rate centered on BARRs (top) and SWRs (bottom) for the interneuron in (F). **(H)** Autocorrelogram (top) and waveform (bottom) of an example PV+ interneuron. **(I)** Average normalized firing rate centered on BARRs (top) and SWRs (bottom) for the interneuron in (H). **(J)** Firing rate ratio during theta versus non-theta periods for BARR+ and putative PV+ interneurons ($p < 0.001$). **(K)** Left, histology of an Sncg-Flp mouse injected with Flp-dependent EYFP-ChR2 (Sncg+ cells are shown in yellow) in CA1. Right, example of optotagging of an Sncg+ interneuron with ChR2 excitation. Black curve shows average firing rate response to blue-light pulses (blue shade) and red lines show shuffled

distribution. Note the atypical response of Sncg+ neurons to light stimulation, also reported by previous papers for CCK+ interneurons (*25*). **(L)** Left, histology of an Sncg-Flp mouse injected with Flp-dependent EYFP-Arch (Sncg+ cells are shown in yellow) in CA1. Right, example of optotagging of an Sncg+ interneuron with Arch3 inhibition. Black curve shows average firing rate response to green-light pulses (green shade) and red lines show shuffled distribution. */**/*** $p < 0.05/0.01/0.001$ Wilcoxon-rank test unless otherwise noted.

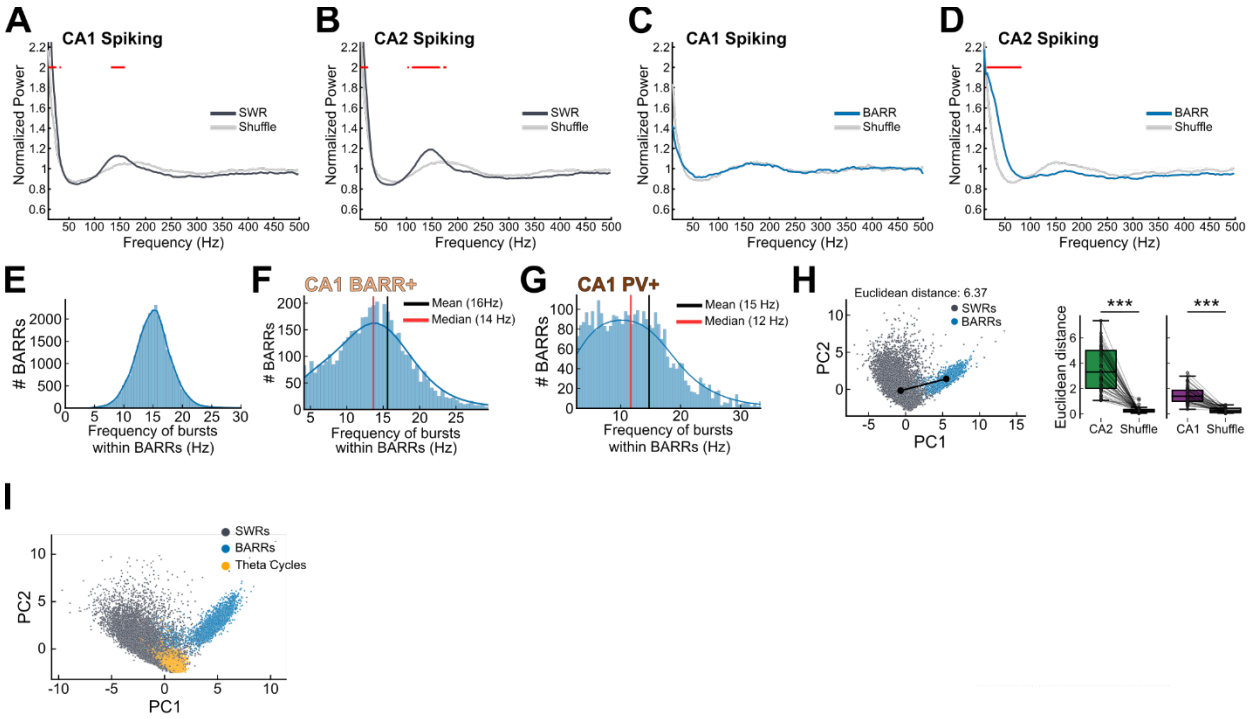

Fig. S4. Bursting frequency and population firing separation between SWRs and BARRs. **(A)** Spectrogram of the population spike train of CA1 units during SWRs (black) and shuffled times (grey). **(B)** Spectrogram of the population spike train of CA2 units during SWRs (black) and shuffled times (grey). **(C)** Spectrogram of the population spike train of CA1 units during BARRs (blue) and shuffled times (grey). **(D)** Spectrogram of the population spike train of CA2 units during BARRs (blue) and shuffled times (grey). **(E)** Burst frequency of CA2 pyramidal cells within BARRs was 15 Hz on average. **(F)** Similar to (A), the burst frequency of CA1 BARR+ interneurons within BARRs was ~15 Hz. **(G)** Burst frequency of CA1 putative PV interneurons within BARRs displayed a skewed distribution with a mean of 15Hz and a median of 12Hz. **(H)** Left: Dimensionality reduction via PCA was carried out on the population firing of CA1 and CA2 pyramidal cells to estimate the Euclidean distance between SWRs and BARRs in 2D PCA space. Right: The distance between SWRs and BARRs was compared against distances calculated from randomized SWR/BARR labels. Both CA2 and CA1 population activity has a greater than chance separation within SWRs and BARRs (CA2: observed versus shuffle: paired t-test, $p < 0.001$. CA1: observed versus shuffle: paired t-test, $p < 0.001$). **(I)** Dimensionality reduction via PCA performed on the population firing of CA1 and CA2 pyramidal cells during SWRs (black, n = 15,084), BARRs (blue, n = 3,289), and theta epochs (orange, n = 5,197). Note how BARR events appear segregated from the rest, indicating they represent distinct population activity patterns. */**/*** $p < 0.05/0.01/0.001$ Wilcoxon-rank test unless otherwise noted.

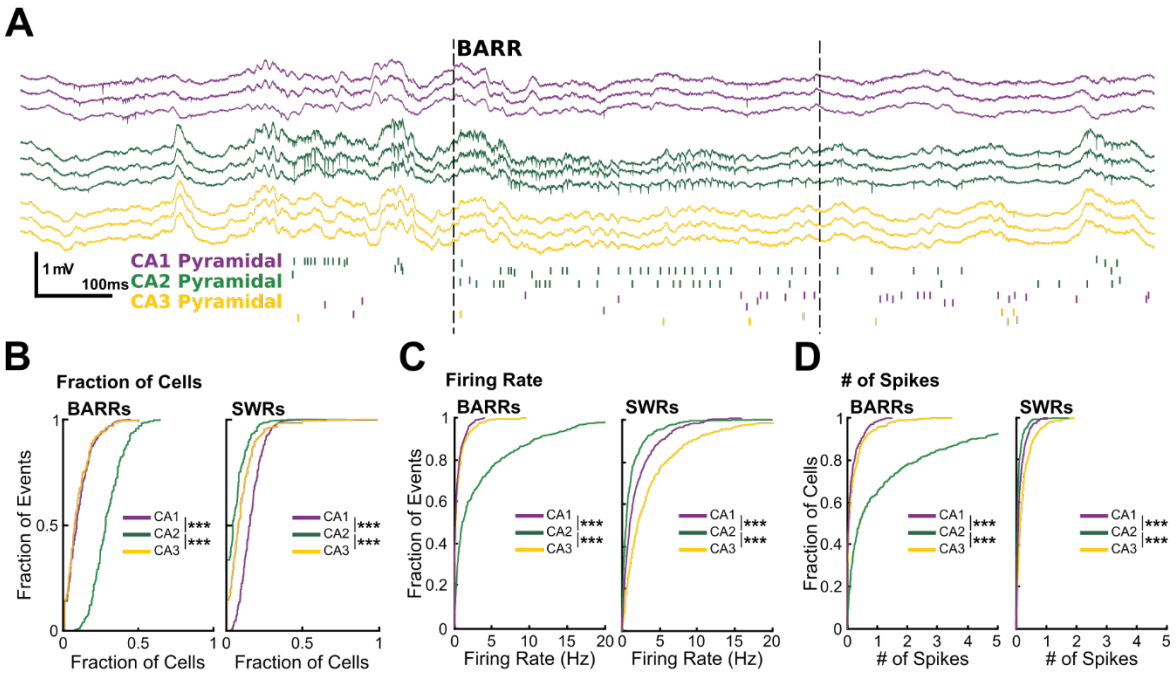

Fig. S5. Single cell properties during SWRs and BARRs in rats performing a spatial learning task. (A) Example of BARRs in rats. **(B)** Cumulative fraction of CA1 (n = 960), CA2 (n = 2137), and CA3 (n = 105) pyramidal cells active in BARRs (left; n = 45,301) and SWRs (right, n = 333,294). Data from n = 5 rats. **(C)** Cumulative firing rate probability of CA1, CA2, and CA3 pyramidal cells during BARRs (left) and SWRs (right). **(D)** Cumulative fraction of CA1, CA2, and CA3 pyramidal cells with different numbers of spikes during BARRs (left) and SWRs (right). */**/*** $p < 0.05/0.01/0.001$ Wilcoxon-rank test unless otherwise noted.

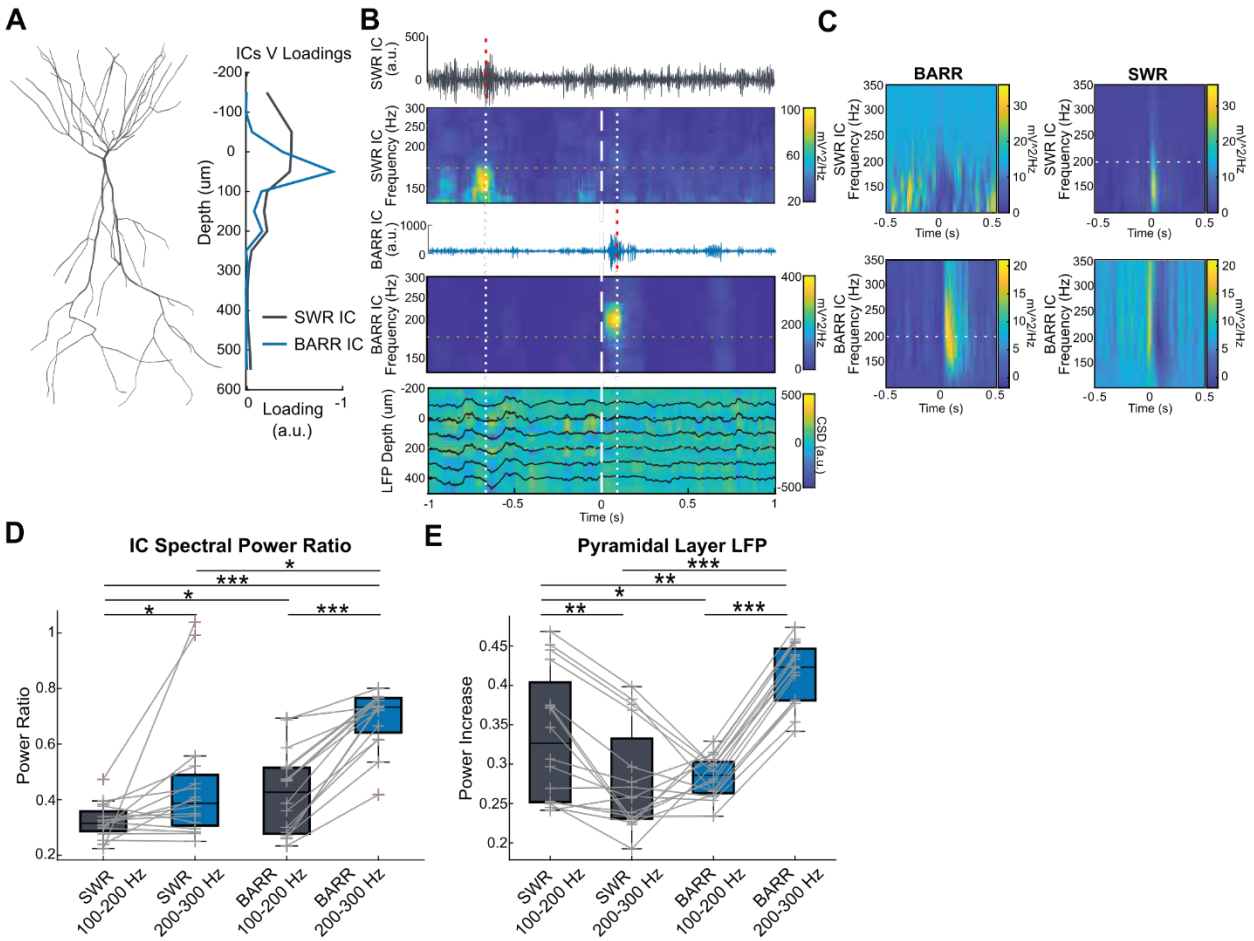

Fig. S6. Independent Component Analysis of BARRs LFPs. (A) Schematic of a CA2 pyramidal cell (left) along with depth profiles of SWR (right, black) and BARR (right, blue) associated main independent components (ICs) extracted with ICA. **(B)** Example of an adjacent BARR and SWR decomposed into SWR IC (top) and BARR IC (middle). Colormaps are spectrograms of each IC. White or red dotted vertical lines indicate the peak of a SWR (towards the left) or BARR (towards the right). The white dashed line indicates the detected onset of the example BARR. Orange horizontal line marks 200 Hz in both colormaps. Note how the SWR IC specifically captures SWR activity at ~150 Hz while the BARR IC captures BARR activity at ~250 Hz. Traces above the spectrogram show high-pass (>100 Hz) filtered source activity of CA2 IC components. CA2 LFP depth profiles for the same window (black traces) are overlayed on top of the current source density (CSD) map (bottom). **(C)** Top, average BARR-triggered spectrum (left, n = 290 events) and SWR-triggered spectrum (right, n = 3172 events) for the SWR IC in an example session. Bottom, average BARR triggered spectrum (left) and SWR triggered spectrum (right) for the BARR IC in the same session. **(D)** Spectral power ratio for SWR and BARR associated independent components in the SWR associated frequency band (100-200 Hz) and BARR associated frequency band (200-300 Hz) (n = 17 sessions in n = 5 rats). **(E)** Pyramidal layer LFP spectral power increase during SWR and BARR events in the SWR and BARR associated frequency bands. */**/*** $p < 0.05/0.01/0.001$ Wilcoxon-rank test unless otherwise noted.

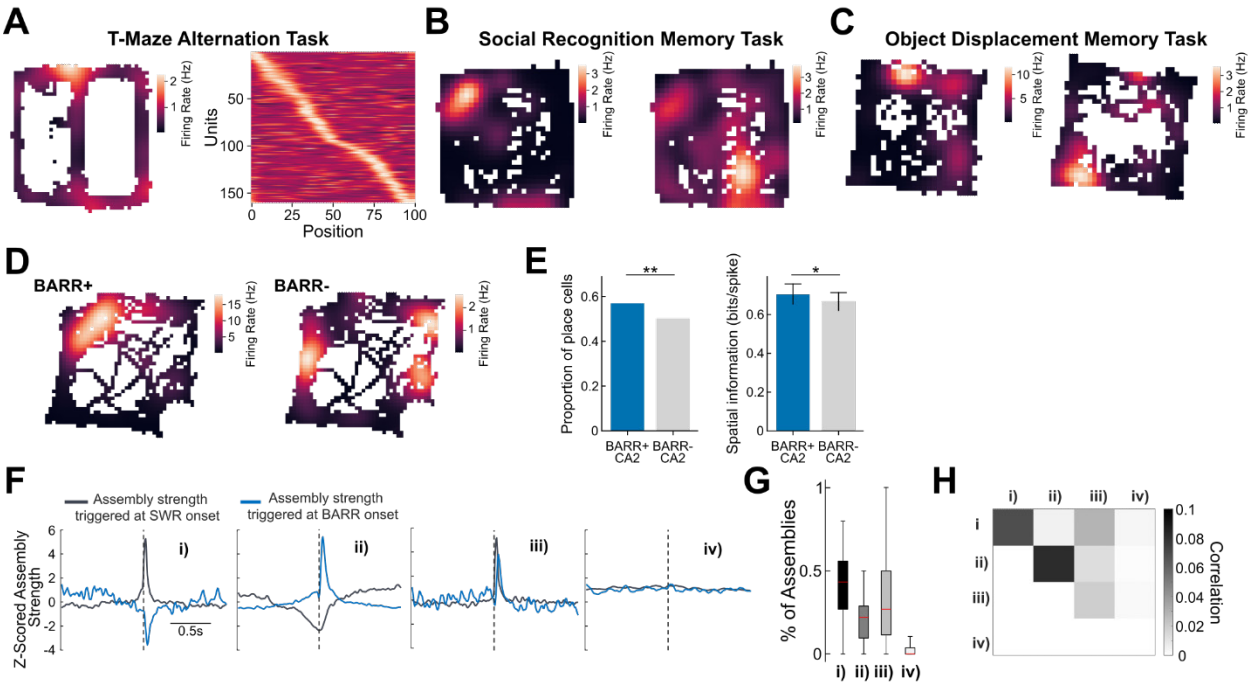

Fig. S7. Place cells in the different tasks and CA2 BARR+/- spatial properties. (A) Example place cell during T-Maze Alternation Task (left) and example session with all place cells covering a whole trajectory of the maze (right). **(B)** Two different example place cells during the Social Recognition Memory Task. **(C)** Two different example place cells during the Object Displacement Memory Task. **(D)** Two different example place cells that were later identified as participating during BARRs (BARR+, left) or not (BARR-, right). **(E)** Proportion of spatially modulated cells from CA2 BARR+/- (left) and spatial information from CA2 BARR+/- (right). **(F)** CA2 pyramidal cell assemblies detected during the task and their associated response during SWRs (grey) and BARRs (blue). CA2 assemblies can be positively modulated by SWRs and negatively modulated by BARRs (i), negatively modulated by SWRs and negatively modulated by BARRs (ii), positively modulated by both SWRs and BARRs (iii), or not modulated by both SWRs and BARRs (iv). **(G)** Proportion of the different types of CA2 assemblies classified as in (F). **(H)** Average correlation of activity patterns during the task for the different types of CA2 assemblies. Note that type i) assemblies have a higher probability to be co-active with other type i) assemblies, as do type ii) assemblies. */**/*** $p < 0.05/0.01/0.001$ Wilcoxon-rank test unless otherwise noted.

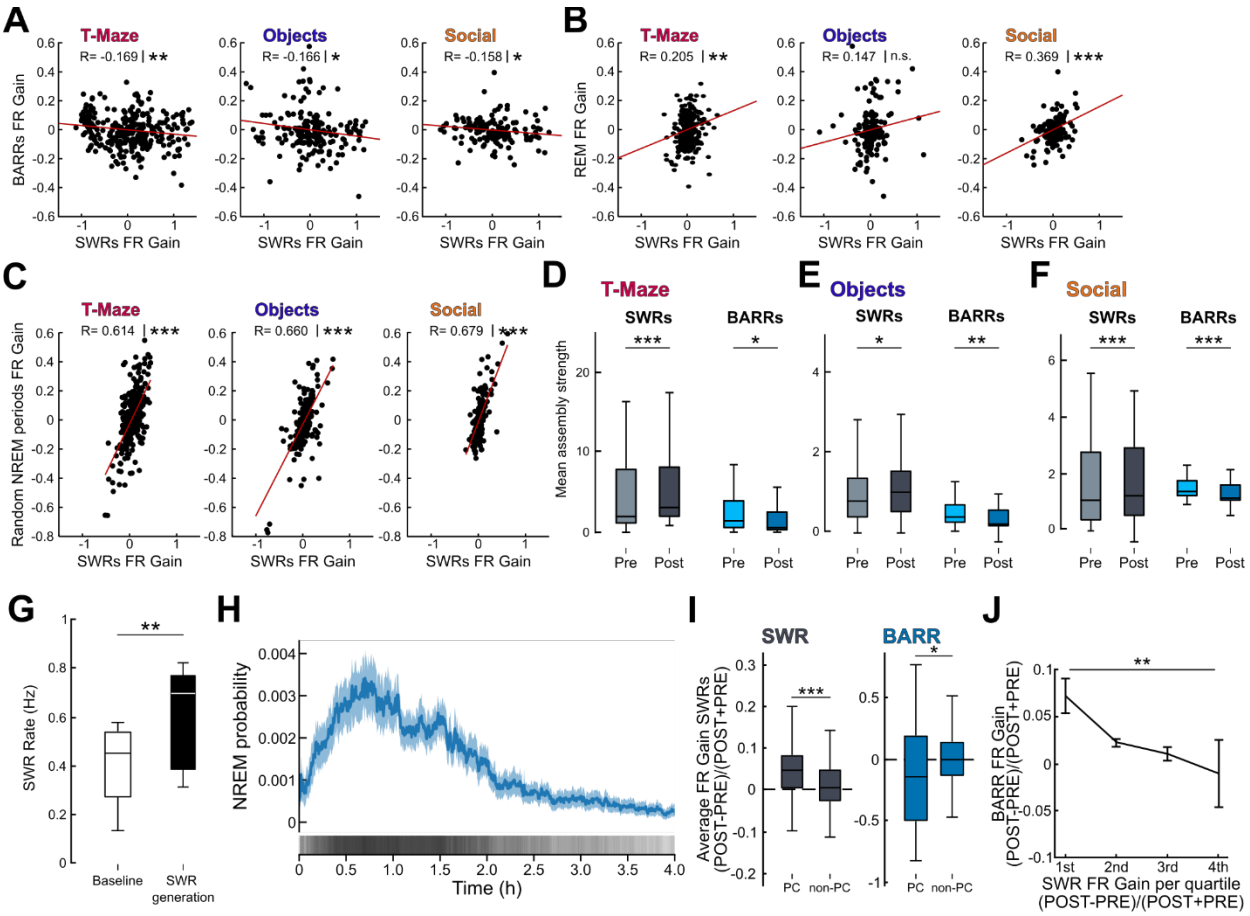

Fig. S8. Firing rate gain during SWRs in relation to other physiologically relevant periods. **(A)** Firing rate gain from pre- to post-sleep BARRs versus SWRs ([POST-PRE]/[POST+PRE]) for T-Maze (left), object displacement task (middle), and social memory task (right). **(B)** Firing rate gain during REM epochs versus SWRs for T-Maze (left), object displacement task (middle), and social memory task (right). **(C)** Firing rate gain during random periods of NREM sleep versus SWRs for T-Maze (left), object displacement task (middle), and social memory task (right). **(D)** Pre- versus post-sleep reactivation during T-Maze ($p < 0.001$ and $p < 0.05$ for SWRs and BARRs, respectively). **(E)** Pre- versus post-sleep reactivation during object displacement task ($p < 0.05$ and $p < 0.01$ for SWRs and BARRs, respectively). **(F)** Pre- versus post-sleep reactivation during the social memory task ($p < 0.001$ and $p < 0.001$ for SWRs and BARRs, respectively), n = 14 sessions from 4 mice for T-Maze, n = 23 sessions from 8 mice for object displacement and n = 16 sessions from 7 mice for social memory from (A) to (F). **(G)** SWR rate during baseline versus ChR2-CamKII stimulation periods ($p < 0.01$, n= 9 sessions in n= 4 mice). Note higher rate during CamKII-ChR2 stimulation periods. **(H)** Average distribution of NREM sleep within the post-task recording sessions (n = 52 sessions in n = 10 mice). **(I)** Firing rate gain from pre- to post-sleep SWRs and BARRs for place cells (n = 115) and non-place cells (n = 176) in rats (n = 5) ($p < 0.001$ and $p < 0.05$ for PC versus non-PC comparison during SWRs and BARRs respectively; Wilcoxon rank-sum test). **(J)** Firing rate gain from pre- to post-sleep BARRs versus SWRs (quartiles) for CA1 pyramidal cells in rats ($p < 0.01$, linear correlation, n = 708). */**/*** $p < 0.05/0.01/0.001$ Wilcoxon-rank test unless otherwise noted.

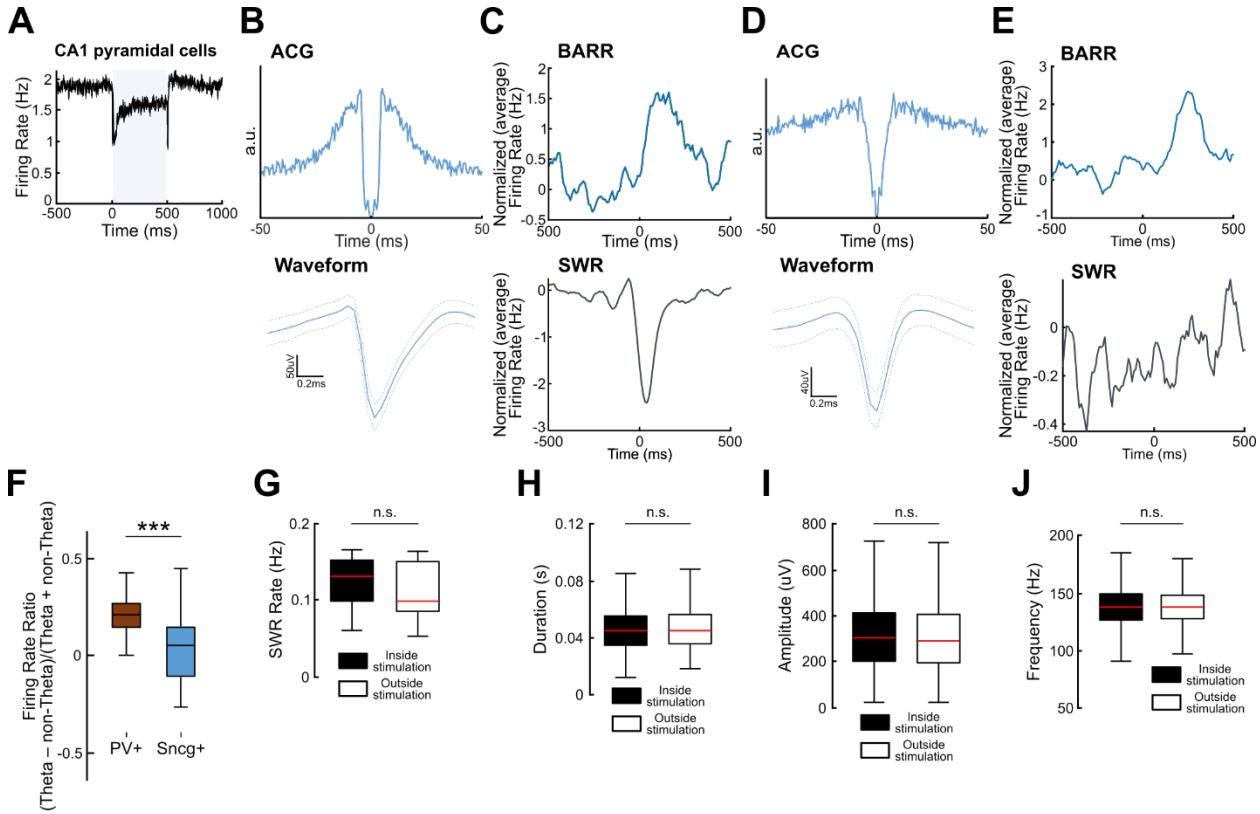

Fig. S9. Sncg+ optotagged cells and SWR properties during Sncg+ silencing. (A) Population of CA1 pyramidal cells for one session during Sncg+ stimulation. Note strong inhibition of CA1. **(B)** Autocorrelogram (top) and waveform (bottom) of an example Sncg+ optotagged cell. **(C)** Average response during BARRs (top) and SWRs (bottom) for the cell shown in (B). **(D)** Autocorrelogram (top) and waveform (bottom) of an example Sncg+ optotagged cell. **(E)** Average response during BARRs (top) and SWRs (bottom) for the cell shown in (D). **(F)** Firing rate ratio during theta versus non-theta periods for Sncg+ and putative PV+ interneurons ($p < 0.001$). **(G)** SWR rate within pulses versus outside pulses ($p > 0.05$). **(H)** SWR duration within pulses versus outside pulses ($p > 0.05$). **(I)** SWR amplitude within pulses versus outside pulses ($p > 0.05$). **(J)** SWR frequency within pulses versus outside pulses ($p > 0.05$). */**/*** $p <$ 0.05/0.01/0.001 Wilcoxon-rank test unless otherwise noted.

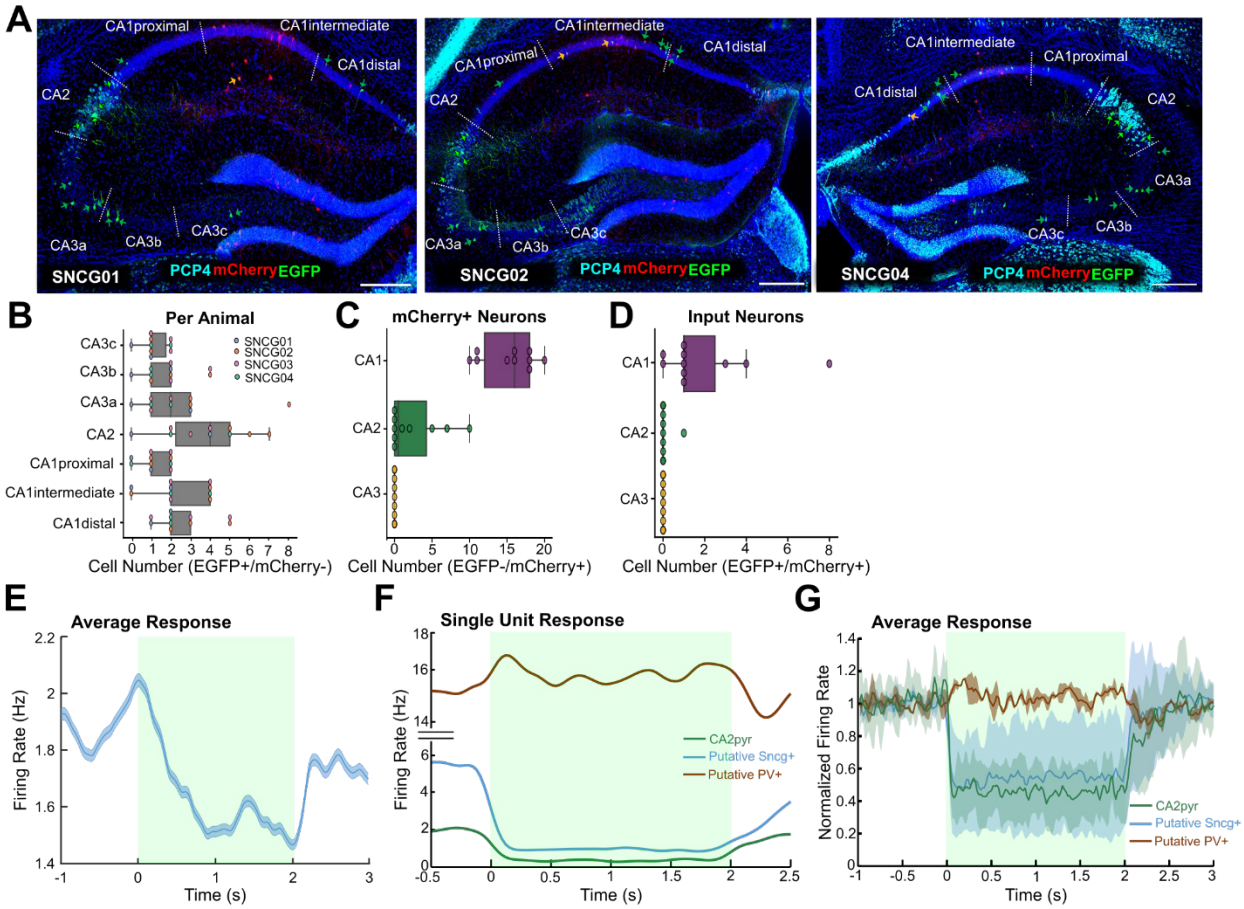

Fig. S10. Example images and expression of input neurons per animal, mCherry-positive neurons, and starter neurons for rabies tracing. (A) Representative examples from different mice. Input cells onto Sncg+ basket cells, showing AAV infected cells (red), starter cells (yellow), and input cells (green). Dashed lines delimit hippocampal regions. CA2 is labeled in cyan using PCP4. Horizontal bar = 300 um. **(B)** Quantification of cells identified as input neurons (i.e., EGFP+/SNCG- cells) from different subregions of the hippocampus shown per animal. **(C)** Quantification of AAV- CAG-FLEx(FRT)-TC mCherry+ neurons in each hippocampal subregion. **(D)** Quantification of starter neurons (i.e. EGPF+/SNCG+) from each hippocampal subregion. **(E)** Average population response of Sncg+ cells to green light pulses (green shading) in an example session from an Sncg-Flp mouse injected with Flp-dependent Arch3. **(F)** Example single unit response to green light pulses (green shading) from various neuron subtypes in an Amigo2-Cre mouse injected with Cre-dependent Arch3. Note the silencing of putative Sncg+ cells but not putative PV+ interneurons during the inhibition of CA2 pyramidal cells. **(G)** Average population response of different neuron subtypes to green light pulses (green shading) in four sessions from two animals (Amigo2-Cre mice injected with Cre-dependent Arch3).

References and Notes

1. W. B. Scoville, B. Milner, Loss of recent memory after bilateral hippocampal lesions. *J. Neurol. Neurosurg. Psychiatry* **20**, 11–21 (1957). doi:10.1136/jnnp.20.1.11 Medline

2. P. Andersen, R. Morris, D. Amaral, T. Bliss, J. O'Keefe, Eds., *The Hippocampus Book* (Oxford Univ. Press, 2007).

3. S. Diekelmann, J. Born, The memory function of sleep. *Nat. Rev. Neurosci.* **11**, 114–126 (2010). doi:10.1038/nrn2762 Medline

4. M. A. Wilson, B. L. McNaughton, Reactivation of hippocampal ensemble memories during sleep. *Science* **265**, 676–679 (1994). doi:10.1126/science.8036517 Medline

5. H. S. Kudrimoti, C. A. Barnes, B. L. McNaughton, Reactivation of hippocampal cell assemblies: Effects of behavioral state, experience, and EEG dynamics. *J. Neurosci.* **19**, 4090–4101 (1999). doi:10.1523/JNEUROSCI.19-10-04090.1999 Medline

6. A. K. Lee, M. A. Wilson, Memory of sequential experience in the hippocampus during slow wave sleep. *Neuron* **36**, 1183–1194 (2002). doi:10.1016/S0896-6273(02)01096-6 Medline

7. A. D. Grosmark, G. Buzsáki, Diversity in neural firing dynamics supports both rigid and learned hippocampal sequences. *Science* **351**, 1440–1443 (2016). doi:10.1126/science.aad1935 Medline

8. B. Giri, H. Miyawaki, K. Mizuseki, S. Cheng, K. Diba, Hippocampal Reactivation Extends for Several Hours Following Novel Experience. *J. Neurosci.* **39**, 866–875 (2019). doi:10.1523/JNEUROSCI.1950-18.2018 Medline

9. G. Girardeau, K. Benchenane, S. I. Wiener, G. Buzsáki, M. B. Zugaro, Selective suppression of hippocampal ripples impairs spatial memory. *Nat. Neurosci.* **12**, 1222–1223 (2009). doi:10.1038/nn.2384 Medline

10. V. Ego-Stengel, M. A. Wilson, Disruption of ripple-associated hippocampal activity during rest impairs spatial learning in the rat. *Hippocampus* **20**, 1–10 (2010). doi:10.1002/hipo.20707 Medline

11. A. Oliva, A. Fernández-Ruiz, F. Leroy, S. A. Siegelbaum, Hippocampal CA2 sharp-wave ripples reactivate and promote social memory. *Nature* **587**, 264–269 (2020). doi:10.1038/s41586-020-2758-y Medline

12. A. Oliva, A. Fernández-Ruiz, G. Buzsáki, A. Berényi, Role of Hippocampal CA2 Region in Triggering Sharp-Wave Ripples. *Neuron* **91**, 1342–1355 (2016). doi:10.1016/j.neuron.2016.08.008 Medline

13. J. Csicsvari, H. Hirase, A. Czurkó, A. Mamiya, G. Buzsáki, Oscillatory coupling of hippocampal pyramidal cells and interneurons in the behaving Rat. *J. Neurosci.* **19**, 274–287 (1999). doi:10.1523/JNEUROSCI.19-01-00274.1999 Medline

14. K. Kay, M. Sosa, J. E. Chung, M. P. Karlsson, M. C. Larkin, L. M. Frank, A hippocampal network for spatial coding during immobility and sleep. *Nature* **531**, 185–190 (2016). doi:10.1038/nature17144 Medline

15. A. Fernández-Ruiz, A. Oliva, M. Soula, F. Rocha-Almeida, G. A. Nagy, G. Martin-Vazquez, G. Buzsáki, Gamma rhythm communication between entorhinal cortex and dentate gyrus

neuronal assemblies. *Science* **372**, eabf3119 (2021). doi:10.1126/science.abf3119 Medline

16. M. Valero, T. J. Viney, R. Machold, S. Mederos, I. Zutshi, B. Schuman, Y. Senzai, B. Rudy, G. Buzsáki, Sleep down state-active ID2/Nkx2.1 interneurons in the neocortex. *Nat. Neurosci.* **24**, 401–411 (2021). doi:10.1038/s41593-021-00797-6 Medline

17. L. Genzel, E. Schut, T. Schröder, R. Eichler, M. Khamassi, A. Gomez, I. Navarro Lobato, F. Battaglia, The object space task shows cumulative memory expression in both mice and rats. *PLOS Biol.* **17**, e3000322 (2019). doi:10.1371/journal.pbio.3000322 Medline

18. D. Dupret, J. O'Neill, B. Pleydell-Bouverie, J. Csicsvari, The reorganization and reactivation of hippocampal maps predict spatial memory performance. *Nat. Neurosci.* **13**, 995–1002 (2010). doi:10.1038/nn.2599 Medline

19. R. E. Harvey, H. L. Robinson, C. Liu, A. Oliva, A. Fernandez-Ruiz, Hippocampo-cortical circuits for selective memory encoding, routing, and replay. *Neuron* **111**, 2076–2090.e9 (2023). doi:10.1016/j.neuron.2023.04.015 Medline

20. C. Liu, R. Todorova, W. Tang, A. Oliva, A. Fernandez-Ruiz, Associative and predictive hippocampal codes support memory-guided behaviors. *Science* **382**, eadi8237 (2023). doi:10.1126/science.adi8237 Medline

21. E. Stark, L. Roux, R. Eichler, Y. Senzai, S. Royer, G. Buzsáki, Pyramidal cell-interneuron interactions underlie hippocampal ripple oscillations. *Neuron* **83**, 467–480 (2014). doi:10.1016/j.neuron.2014.06.023 Medline

22. A. Fernández-Ruiz, A. Oliva, E. Fermino de Oliveira, F. Rocha-Almeida, D. Tingley, G. Buzsáki, Long-duration hippocampal sharp wave ripples improve memory. *Science* **364**, 1082–1086 (2019). doi:10.1126/science.aax0758 Medline

23. J. Gan, S. M. Weng, A. J. Pernía-Andrade, J. Csicsvari, P. Jonas, Phase-Locked Inhibition, but Not Excitation, Underlies Hippocampal Ripple Oscillations in Awake Mice In Vivo. *Neuron* **93**, 308–314 (2017). doi:10.1016/j.neuron.2016.12.018 Medline

24. D. F. English, A. Peyrache, E. Stark, L. Roux, D. Vallentin, M. A. Long, G. Buzsáki, Excitation and inhibition compete to control spiking during hippocampal ripples: Intracellular study in behaving mice. *J. Neurosci.* **34**, 16509–16517 (2014). doi:10.1523/JNEUROSCI.2600-14.2014 Medline

25. B. Dudok, P. M. Klein, E. Hwaun, B. R. Lee, Z. Yao, O. Fong, J. C. Bowler, S. Terada, F. T. Sparks, G. G. Szabo, J. S. Farrell, J. Berg, T. L. Daigle, B. Tasic, J. Dimidschstein, G. Fishell, A. Losonczy, H. Zeng, I. Soltesz, Alternating sources of perisomatic inhibition during behavior. *Neuron* **109**, 997–1012.e9 (2021). doi:10.1016/j.neuron.2021.01.003 Medline

26. B. Vancura, T. Geiller, A. Grosmark, V. Zhao, A. Losonczy, Inhibitory control of sharp-wave ripple duration during learning in hippocampal recurrent networks. *Nat. Neurosci.* **26**, 788–797 (2023). doi:10.1038/s41593-023-01306-7 Medline

27. G. F. Turi, W.-K. Li, S. Chavlis, I. Pandi, J. O'Hare, J. B. Priestley, A. D. Grosmark, Z. Liao, M. Ladow, J. F. Zhang, B. V. Zemelman, P. Poirazi, A. Losonczy, Vasoactive Intestinal Polypeptide-Expressing Interneurons in the Hippocampus Support Goal-Oriented Spatial Learning. *Neuron* **101**, 1150–1165.e8 (2019). doi:10.1016/j.neuron.2019.01.009 Medline

28. L. A. Schwarz, K. Miyamichi, X. J. Gao, K. T. Beier, B. Weissbourd, K. E. DeLoach, J. Ren, S. Ibanes, R. C. Malenka, E. J. Kremer, L. Luo, Viral-genetic tracing of the input-output organization of a central noradrenaline circuit. *Nature* **524**, 88–92 (2015). doi:10.1038/nature14600 Medline

29. K. Miyamichi, Y. Shlomai-Fuchs, M. Shu, B. C. Weissbourd, L. Luo, A. Mizrahi, Dissecting local circuits: Parvalbumin interneurons underlie broad feedback control of olfactory bulb output. *Neuron* **80**, 1232–1245 (2013). doi:10.1016/j.neuron.2013.08.027 Medline

30. I. R. Wickersham, D. C. Lyon, R. J. O. Barnard, T. Mori, S. Finke, K.-K. Conzelmann, J. A. T. Young, E. M. Callaway, Monosynaptic restriction of transsynaptic tracing from single, genetically targeted neurons. *Neuron* **53**, 639–647 (2007). doi:10.1016/j.neuron.2007.01.033 Medline

31. D. F. English, S. McKenzie, T. Evans, K. Kim, E. Yoon, G. Buzsáki, Pyramidal Cell-Interneuron Circuit Architecture and Dynamics in Hippocampal Networks. *Neuron* **96**, 505–520.e7 (2017). doi:10.1016/j.neuron.2017.09.033 Medline

32. D. K. Rangel Guerrero, K. Balueva, U. Barayeu, P. Baracskay, I. Gridchyn, M. Nardin, C. N. Roth, P. Wulff, J. Csicsvari, Hippocampal cholecystokinin-expressing interneurons regulate temporal coding and contextual learning. *Neuron* **112**, 2045–2061.e10 (2024). doi:10.1016/j.neuron.2024.03.019 Medline

33. M. Valero, R. G. Averkin, I. Fernandez-Lamo, J. Aguilar, D. Lopez-Pigozzi, J. R. Brotons-Mas, E. Cid, G. Tamas, L. Menendez de la Prida, Mechanisms for Selective Single-Cell Reactivation during Offline Sharp-Wave Ripples and Their Distortion by Fast Ripples. *Neuron* **94**, 1234–1247.e7 (2017). doi:10.1016/j.neuron.2017.05.032 Medline

34. J. N. Gelinas, D. Khodagholy, T. Thesen, O. Devinsky, G. Buzsáki, Interictal epileptiform discharges induce hippocampal-cortical coupling in temporal lobe epilepsy. *Nat. Med.* **22**, 641–648 (2016). doi:10.1038/nm.4084 Medline

35. G. Tononi, C. Cirelli, Sleep and synaptic homeostasis: A hypothesis. *Brain Res. Bull.* **62**, 143–150 (2003). doi:10.1016/j.brainresbull.2003.09.004 Medline

36. G. G. Turrigiano, K. R. Leslie, N. S. Desai, L. C. Rutherford, S. B. Nelson, Activity-dependent scaling of quantal amplitude in neocortical neurons. *Nature* **391**, 892–896 (1998). doi:10.1038/36103 Medline

37. V. V. Vyazovskiy, C. Cirelli, M. Pfister-Genskow, U. Faraguna, G. Tononi, Molecular and electrophysiological evidence for net synaptic potentiation in wake and depression in sleep. *Nat. Neurosci.* **11**, 200–208 (2008). doi:10.1038/nn2035 Medline

38. K. B. Hengen, A. Torrado Pacheco, J. N. McGregor, S. D. Van Hooser, G. G. Turrigiano, Neuronal Firing Rate Homeostasis Is Inhibited by Sleep and Promoted by Wake. *Cell* **165**, 180–191 (2016). doi:10.1016/j.cell.2016.01.046 Medline

39. D. Levenstein, J. Gornet, R. Huszár, G. Girardeau, A. Grosmark, A. Peyrache, Y. Senzai, B. O. Watson, K. Mizuseki, J. Rinzel, G. Buzsáki, Distinct ground state and activated state modes of firing in forebrain neurons. bioRxiv 2021.09.20.461152 [Preprint] (2022); https://doi.org/10.1101/2021.09.20.461152.

40. B. O. Watson, D. Levenstein, J. P. Greene, J. N. Gelinas, G. Buzsáki, Network Homeostasis and State Dynamics of Neocortical Sleep. *Neuron* **90**, 839–852 (2016). doi:10.1016/j.neuron.2016.03.036 Medline

41. G. Buzsáki, Hippocampal sharp wave-ripple: A cognitive biomarker for episodic memory and planning. *Hippocampus* **25**, 1073–1188 (2015). doi:10.1002/hipo.22488 Medline

42. H. Norimoto, K. Makino, M. Gao, Y. Shikano, K. Okamoto, T. Ishikawa, T. Sasaki, H. Hioki, S. Fujisawa, Y. Ikegaya, Hippocampal ripples down-regulate synapses. *Science* **359**, 1524–1527 (2018). doi:10.1126/science.aao0702 Medline

43. D. Cavalieri, A. Angelova, A. Islah, C. Lopez, M. Bocchio, Y. Bollmann, A. Baude, R. Cossart, CA1 pyramidal cell diversity is rooted in the time of neurogenesis. *eLife* **10**, e69270 (2021). doi:10.7554/eLife.69270 Medline

44. R. Huszár, Y. Zhang, H. Blockus, G. Buzsáki, Preconfigured dynamics in the hippocampus are guided by embryonic birthdate and rate of neurogenesis. *Nat. Neurosci.* **25**, 1201–1212 (2022). doi:10.1038/s41593-022-01138-x Medline

45. K. Mizuseki, K. Diba, E. Pastalkova, G. Buzsáki, Hippocampal CA1 pyramidal cells form functionally distinct sublayers. *Nat. Neurosci.* **14**, 1174–1181 (2011). doi:10.1038/nn.2894 Medline

46. M. Valero, E. Cid, R. G. Averkin, J. Aguilar, A. Sanchez-Aguilera, T. J. Viney, D. Gomez-Dominguez, E. Bellistri, L. M. de la Prida, Determinants of different deep and superficial CA1 pyramidal cell dynamics during sharp-wave ripples. *Nat. Neurosci.* **18**, 1281–1290 (2015). doi:10.1038/nn.4074 Medline

47. N. B. Danielson, J. D. Zaremba, P. Kaifosh, J. Bowler, M. Ladow, A. Losonczy, Sublayer-Specific Coding Dynamics during Spatial Navigation and Learning in Hippocampal Area CA1. *Neuron* **91**, 652–665 (2016). doi:10.1016/j.neuron.2016.06.020 Medline

48. D. Schlingloff, S. Káli, T. F. Freund, N. Hájos, A. I. Gulyás, Mechanisms of sharp wave initiation and ripple generation. *J. Neurosci.* **34**, 11385–11398 (2014). doi:10.1523/JNEUROSCI.0867-14.2014 Medline

49. M. Bartos, C. Elgueta, Functional characteristics of parvalbumin- and cholecystokinin-expressing basket cells. *J. Physiol.* **590**, 669–681 (2012). doi:10.1113/jphysiol.2011.226175 Medline

50. B. Dudok, L. Z. Fan, J. S. Farrell, S. Malhotra, J. Homidan, D. K. Kim, C. Wenardy, C. Ramakrishnan, Y. Li, K. Deisseroth, I. Soltesz, Retrograde endocannabinoid signaling at inhibitory synapses in vivo. *Science* **383**, 967–970 (2024). doi:10.1126/science.adk3863 Medline

51. V. Chevaleyre, P. E. Castillo, Heterosynaptic LTD of hippocampal GABAergic synapses: A novel role of endocannabinoids in regulating excitability. *Neuron* **38**, 461–472 (2003). doi:10.1016/S0896-6273(03)00235-6 Medline

52. S. McKenzie, R. Huszár, D. F. English, K. Kim, F. Christensen, E. Yoon, G. Buzsáki, Preexisting hippocampal network dynamics constrain optogenetically induced place fields. *Neuron* **109**, 1040–1054.e7 (2021). doi:10.1016/j.neuron.2021.01.011 Medline

53. R. Harvey, R. Todorova, L. A. Karaba, A. Fernandez-Ruiz, H. L. Robinson, A. Oliva, C. Liu, L. Berkowitz, P. Paudel, M. T. Romero-Barragan, ayalab1/neurocode: Release, version v1.0.0, Zenodo (2023); https://doi.org/10.5281/zenodo.7819979.

54. F. L. Hitti, S. A. Siegelbaum, The hippocampal CA2 region is essential for social memory. *Nature* **508**, 88–92 (2014). doi:10.1038/nature13028 Medline

55. M. Matsuyama, Y. Ohashi, T. Tsubota, M. Yaguchi, S. Kato, K. Kobayashi, Y. Miyashita, Avian sarcoma leukosis virus receptor-envelope system for simultaneous dissection of multiple neural circuits in mammalian brain. *Proc. Natl. Acad. Sci. U.S.A.* **112**, E2947–E2956 (2015). doi:10.1073/pnas.1423963112 Medline

56. L. E. Fenno, C. Ramakrishnan, Y. S. Kim, K. E. Evans, M. Lo, S. Vesuna, M. Inoue, K. Y. M. Cheung, E. Yuen, N. Pichamoorthy, A. S. O. Hong, K. Deisseroth, Comprehensive Dual- and Triple-Feature Intersectional Single-Vector Delivery of Diverse Functional Payloads to Cells of Behaving Mammals. *Neuron* **107**, 836–853.e11 (2020). doi:10.1016/j.neuron.2020.06.003 Medline

57. L. E. Fenno, J. Mattis, C. Ramakrishnan, M. Hyun, S. Y. Lee, M. He, J. Tucciarone, A. Selimbeyoglu, A. Berndt, L. Grosenick, K. A. Zalocusky, H. Bernstein, H. Swanson, C. Perry, I. Diester, F. M. Boyce, C. E. Bass, R. Neve, Z. J. Huang, K. Deisseroth, Targeting cells with single vectors using multiple-feature Boolean logic. *Nat. Methods* **11**, 763–772 (2014). doi:10.1038/nmeth.2996 Medline

58. B. Y. Chow, X. Han, A. S. Dobry, X. Qian, A. S. Chuong, M. Li, M. A. Henninger, G. M. Belfort, Y. Lin, P. E. Monahan, E. S. Boyden, High-performance genetically targetable optical neural silencing by light-driven proton pumps. *Nature* **463**, 98–102 (2010). doi:10.1038/nature08652 Medline

59. A. Mathis, P. Mamidanna, K. M. Cury, T. Abe, V. N. Murthy, M. W. Mathis, M. Bethge, DeepLabCut: Markerless pose estimation of user-defined body parts with deep learning. *Nat. Neurosci.* **21**, 1281–1289 (2018). doi:10.1038/s41593-018-0209-y Medline

60. E. Stark, L. Roux, R. Eichler, G. Buzsáki, Local generation of multineuronal spike sequences in the hippocampal CA1 region. *Proc. Natl. Acad. Sci. U.S.A.* **112**, 10521–10526 (2015). doi:10.1073/pnas.1508785112 Medline

61. K. Kohara, M. Pignatelli, A. J. Rivest, H.-Y. Jung, T. Kitamura, J. Suh, D. Frank, K. Kajikawa, N. Mise, Y. Obata, I. R. Wickersham, S. Tonegawa, Cell type-specific genetic and optogenetic tools reveal hippocampal CA2 circuits. *Nat. Neurosci.* **17**, 269–279 (2014). doi:10.1038/nn.3614 Medline

62 M. Pachitariu, N. A. Steinmetz, S. N. Kadir, M. Carandini, K. D. Harris, "Fast and accurate spike sorting of high-channel count probes with KiloSort" in *Advances in Neural Information Processing Systems*, D. Lee, M. Sugiyama, U. Luxburg, I. Guyon, R. Garnett, Eds. (NeurIPS, 2016), vol. 29, pp. 4448–4456.

63. P. C. Petersen, J. H. Siegle, N. A. Steinmetz, S. Mahallati, G. Buzsáki, CellExplorer: A framework for visualizing and characterizing single neurons. *Neuron* **109**, 3594–3608.e2 (2021). doi:10.1016/j.neuron.2021.09.002 Medline

64. A. Sirota, S. Montgomery, S. Fujisawa, Y. Isomura, M. Zugaro, G. Buzsáki, Entrainment of neocortical neurons and gamma oscillations by the hippocampal theta rhythm. *Neuron* **60**, 683–697 (2008). doi:10.1016/j.neuron.2008.09.014 Medline

65. G. Girardeau, I. Inema, G. Buzsáki, Reactivations of emotional memory in the hippocampus-amygdala system during sleep. *Nat. Neurosci.* **20**, 1634–1642 (2017). doi:10.1038/nn.4637 Medline

66. V. Lopes-dos-Santos, S. Ribeiro, A. B. L. Tort, Detecting cell assemblies in large neuronal populations. *J. Neurosci. Methods* **220**, 149–166 (2013). doi:10.1016/j.jneumeth.2013.04.010 Medline

67. G. M. van de Ven, S. Trouche, C. G. McNamara, K. Allen, D. Dupret, Hippocampal Offline Reactivation Consolidates Recently Formed Cell Assembly Patterns during Sharp Wave-Ripples. *Neuron* **92**, 968–974 (2016). doi:10.1016/j.neuron.2016.10.020 Medline

68. K. D. Harris, H. Hirase, X. Leinekugel, D. A. Henze, G. Buzsáki, Temporal interaction between single spikes and complex spike bursts in hippocampal pyramidal cells. *Neuron* **32**, 141–149 (2001). doi:10.1016/S0896-6273(01)00447-0 Medline

69. C. Torrence, G. P. Compo, A Practical Guide to Wavelet Analysis. *Bull. Am. Meteorol. Soc.* **79**, 61–78 (1998). doi:10.1175/1520-0477(1998)079<0061:APGTWA>2.0.CO;2

70. E. W. Schomburg, A. Fernández-Ruiz, K. Mizuseki, A. Berényi, C. A. Anastassiou, C. Koch, G. Buzsáki, Theta phase segregation of input-specific gamma patterns in entorhinal-hippocampal networks. *Neuron* **84**, 470–485 (2014). doi:10.1016/j.neuron.2014.08.051 Medline

71. Y. Senzai, A. Fernandez-Ruiz, G. Buzsáki, Layer-Specific Physiological Features and Interlaminar Interactions in the Primary Visual Cortex of the Mouse. *Neuron* **101**, 500–513.e5 (2019). doi:10.1016/j.neuron.2018.12.009 Medline

72. G. Martín-Vázquez, T. Asabuki, Y. Isomura, T. Fukai, Learning Task-Related Activities From Independent Local-Field-Potential Components Across Motor Cortex Layers. *Front. Neurosci.* **12**, 429 (2018). doi:10.3389/fnins.2018.00429 Medline

73. A. Hyvärinen, E. Oja, Independent component analysis: Algorithms and applications. *Neural Netw.* **13**, 411–430 (2000). doi:10.1016/S0893-6080(00)00026-5 Medline

74. P. Mitra, H. Bokil, *Observed Brain Dynamics* (Oxford University Press, 2007).

75. K. Zhang, L.-W. Chan, An Adaptive Method for Subband Decomposition ICA. *Neural Comput.* **18**, 191–223 (2006). doi:10.1162/089976606774841620

76. A. D. Grosmark, K. Mizuseki, E. Pastalkova, K. Diba, G. Buzsáki, REM sleep reorganizes hippocampal excitability. *Neuron* **75**, 1001–1007 (2012). doi:10.1016/j.neuron.2012.08.015 Medline

77. L. Roux, B. Hu, R. Eichler, E. Stark, G. Buzsáki, Sharp wave ripples during learning stabilize the hippocampal spatial map. *Nat. Neurosci.* **20**, 845–853 (2017). doi:10.1038/nn.4543 Medline